CrystEngComm

PAPER

View Article Online
View Journal | View Issue

Published on 13 March 2014. Downloaded by Gebze Institute of Technology on 14/05/2014 15:56:09.

Cite this: *CrystEngComm*, 2014, **16**, 4493

Controlling ZIF-8 nano- and microcrystal formation and reactivity through zinc salt variations†

Aleksandra Schejn,[a] Lavinia Balan,[b] Véronique Falk,[a] Lionel Aranda,[c] Ghouti Medjahdi[c] and Raphaël Schneider*[a]

Received 5th December 2013,
Accepted 12th March 2014

DOI: 10.1039/c3ce42485e

www.rsc.org/crystengcomm

We report here a simple method for controlling the crystal size and morphology of zeolitic imidazolate framework-8 (ZIF-8) nanocrystals in methanol solution. ZIF-8 crystals were prepared by mixing 2-methylimidazole (Hmim) with various zinc salts for 1 h and using a Hmim/Zn(+2) salt molar ratio of 8/1. All products prepared were assigned to a sodalite-type structure and both particle size and morphology were found to be dependent on the reactivity of the Zn(+2) salt. Small ZIF-8 crystals with diameters varying between *ca.* 50 and 200 nm were obtained with reactive zinc salts like $Zn(acac)_2$, $Zn(NO_3)_2$, $ZnSO_4$ or $Zn(ClO_4)_2$ as demonstrated by SEM, TEM and DLS analyses. The use of $ZnCl_2$, $Zn(OAc)_2$ or ZnI_2 afforded crystals with sizes varying between *ca.* 350 and 650 nm. Finally, the low reactive $ZnBr_2$ salt was found to generate microsized crystals. Taking ZIF-8 crystals prepared from $Zn(NO_3)_2$, $Zn(OAc)_2$ and $ZnBr_2$ as representatives and through thermogravimetric analysis and BET measurements, we also demonstrated that changes in particle size induced changes in stability and adsorption properties. The small sized ZIF-8 crystals produced from $Zn(NO_3)_2$ were found to exhibit the highest surface area (1700 $m^2\ g^{-1}$) and the best catalytic activity in Knoevenagel and Friedländer reactions.

Introduction

Metal–organic frameworks (MOFs) are new microporous inorganic–organic hybrid materials that exhibit tunable structures, low density and ultrahigh surface areas. These materials may therefore have various potential applications in catalysis,[1–3] hydrogen storage,[4–6] and CO_2 adsorption.[7,8] Among MOFs, the so-called zeolitic imidazolate frameworks (ZIFs) have recently attracted considerable attention. In these materials, metal atoms such as Zn^{2+} are linked through N atoms by a ditopic imidazolate (im^-) ligand to form neutral frameworks.[9–12] Each Zn^{2+} atom connects four im^- and the $\{Zn^{2+}(im^-)_2\}$ units are analogous to the $\{SiO_2\}$ tetrahedra in zeolites and the Zn–im–Zn bond angle is similar to the Si–O–Si bond angle (145°). Guest-free ZIFs have not only the large surface area and pore volume of classical MOFs but also the high chemical and thermal stability of conventional zeolites.[10,13] Due to these features, ZIFs show great potential for gas storage and separation.[14–18]

ZIF-8 ($Zn(mim)_2$, mim = 2-methylimidazole) is the most representative ZIF material with a sodalite zeolite-type topology, in which ZnN_4 tetrahedra are connected through imidazolate linkers forming cages 11.6 Å in diameter which are accessible through a narrow six-ring pore (3.4 Å).[13] ZIF-8 has a high thermal stability (550 °C in N_2), large surface area (BET: 1630–1700 $m^2\ g^{-1}$),[13] and a high chemical resistance to various solvents.[19,20] All of these properties are outstanding among MOFs, making ZIF-8 an ideal candidate for numerous industrial applications. Nevertheless, to open the way for applications such as sensors, catalysts or as materials for gas separation, a real effort has to be made on shaping the ZIF-8 hybrid frameworks. Variation of morphology and size of ZIF-8 crystals is of great importance because these parameters can markedly affect the functional properties and performance of these nanomaterials. Moreover, controlling the shape and size of ZIF nanoparticles may not only provide a fundamental understanding of the crystallisation mechanisms but could also improve structural and morphological control in the synthesis of these novel porous materials. However, these important issues have only scarcely been addressed in the field of ZIF-8 nanomaterials.

[a] *Université de Lorraine, Laboratoire Réactions et Génie des Procédés (LRGP), UMR 7274, CNRS, 1 rue Grandville, BP 20451, 54001 Nancy Cedex, France. E-mail: raphael.schneider@univ-lorraine.fr; Tel: +33 3 83 17 50 53*
[b] *Institut de Science des Matériaux de Mulhouse (IS2M), UMR 7361, 15 rue Jean Starcky, 68093 Mulhouse, France*
[c] *Université de Lorraine, Institut Jean Lamour (IJL), UMR 7198, CNRS, Vandoeuvre-lès-Nancy Cedex, BP 70239, 54506, France*

† Electronic supplementary information (ESI) available: Size distributions of ZIF-8 crystals and XRD patterns of ZnO crystals produced by thermal decomposition of ZIF-8. See DOI: 10.1039/c3ce42485e

Published on 13 March 2014. Downloaded by Gebze Institute of Technology on 14/05/2014 15:56:09.

In recent years, different strategies have been adopted to manipulate the morphology and size of ZIF-8 crystals. Variation of synthetic parameters including solvent, concentration and molar ratio of reactants, temperature and duration can markedly affect the size of the crystals.[21,22] An excess of the bridging ligand relative to the zinc salt is generally employed to increase the nucleation rate. Addition of sodium formate that acts as a base in the deprotonation equilibrium of mim in the reaction medium was found to influence the crystal shape and size of ZIF-8 nanoparticles.[23,24] Surfactants such as poly(diallyldimethylammonium chloride)[25] or cetyltrimethylammonium bromide[26] or the gelatin biopolymer[27] have also been used as growth inhibitors to limit the ZIF-8 crystal size or to tune the crystal morphology. Finally, the use of auxiliary ligands such as amines or carboxylates acting as competitors to the mim bridging ligand can also modulate the crystallisation process and thus the particle size and morphology.[21]

Variation of zinc salts is largely unexplored for ZIF nanocrystals despite the advantages this offers in terms of simplicity and processability. For $(Zn_4O[(OOC)_2C_6H_4]_3)$ (MOF-5), the influence of the zinc precursor on the morphology and size of nanocrystals produced was demonstrated by Biemmi *et al.*[28] Very recently, Torad *et al.* showed that replacing $Zn(NO_3)_2$ with $Zn(OAc)_2$ markedly slowed down the generation speed of ZIF-8 crystals, thus leading to large-sized nanoparticles.[29] The importance of the Zn(+2) precursor was also identified by Zhu *et al.* who discovered that ZnO nanoneedles could be produced during the synthesis of ZIF-8 crystals using zinc carbonate as the zinc source.[30] However, these studies have not yielded more detailed information concerning the influence of the zinc precursor on the size and morphology of ZIF nanocrystals produced.

Here we report a systematic investigation of the influence of the zinc source on the morphology and size of ZIF-8 crystals. All reactions were conducted in methanol at room temperature. Our results demonstrate that the reactivity of the zinc precursor is able to direct the assembly of metal–organic systems such as ZIF-8 nanocrystals and thus their catalytic activity. The surface areas and the thermal stabilities of the networks, determined using the Brunauer–Emmett–Teller (BET) method and thermogravimetric analysis (TGA) respectively, are also reported.

Results and discussion

Methanol is the most commonly used organic solvent for the production of ZIF-8 nanocrystals and was therefore used in the experiments.[21,31] Moreover, methanol only weakly interacts with the ZIF-8 framework and can thus be removed much easier than more polar solvents like DMF.[32] The procedure employs an excess of the bridging Hmim ligand with respect to the Zn(+2) source to increase the nucleation rate and works well at room temperature without the need of any activation. All syntheses were conducted with a molar ratio of Zn/Hmim/MeOH of 1/8/559 in analogy to a previous report[33] and for a duration of 1 h. As recently described,[33] the structural evolution as a function of time for ZIF-8 nanoparticles can be divided into three stages: (i) fast nucleation ($t < 10$ min), (ii) growth stage ($10 < t < 60$ min) during which crystallinity increases with time, and (iii) stationary phase ($t > 60$ min) during which the crystallisation remains constant but ZIF-8 nanoparticles transform into larger ones through Ostwald ripening (a thermodynamically driven process in which small particles disappear at the expense of growing larger ones, which are energetically favored).[34] Therefore, one may assume that the ZIF-8 structure is fully developed after a reaction period of 1 h and the synthesis was then stopped. Products were then collected by centrifugation and washed with methanol several times. Syntheses were conducted with $Zn(NO_3)_2$, $Zn(acac)_2$, $Zn(ClO_4)_2$, $ZnSO_4$, $Zn(OAc)_2$, $ZnCl_2$, $ZnBr_2$ and ZnI_2 in order to gain insight into the reactivity and role of the zinc counterion in changing the morphology and size of ZIF-8 crystals.

Using $ZnSO_4$ or $Zn(acac)_2$, addition of a few droplets of Hmim caused the immediate precipitation of ZIF-8. With $Zn(ClO_4)_2$, the solution became turbid just after the addition of Hmim and precipitates appeared over time. With $Zn(NO_3)_2$ and $ZnCl_2$, the solution became cloudy within 2 min but white precipitates were much dense with $Zn(NO_3)_2$. With these reactive salts, the large amount of deprotonated Hmim (mim^-) accelerates the formation of ZIF-8 *via* a coordination reaction of the Zn cations and mim^-. Using $Zn(OAc)_2$ or ZnI_2, a slower formation rate of ZIF-8 was observed and the colloidal solution formed within 2.5 min. Finally, with $ZnBr_2$, the solution remained transparent at ambient temperature for at least 30 min and then precipitates appeared. These first observations clearly indicate that the Zn precursors may significantly accelerate or slow down the particle formation rate.

Each synthesis yielded pure-phase ZIF-8 crystals as demonstrated by X-ray diffraction (XRD) patterns (Fig. 1). Patterns generated by the ordered porous structure of the ZIF-8 particles between 2θ values of 5 and 40° can be observed

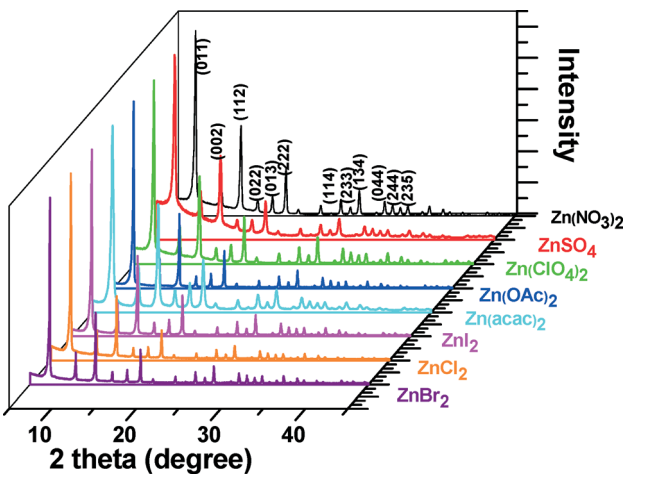

Fig. 1 XRD patterns of ZIF-8 nanocrystals prepared with different zinc precursors.

 This journal is © The Royal Society of Chemistry 2014

Published on 13 March 2014. Downloaded by Gebze Institute of Technology on 14/05/2014 15:56:09.

and the peak broadening observed indicates the formation of nanosized crystals. The relative intensities and prominent peak positions, including 011, 002, 112, 022, 013, and 222 are in good agreement with previous reports,[13,31] confirming the sodalite structure, which is the typical structure of ZIF-8, and the well-defined peaks revealed high crystallinity. The interplanar spacings calculated using Bragg's law from the reflection at different Bragg's angles correspond to a body centered cubic structure with a unit cell parameter of 17 Å and are in accordance with those reported in the literature.

The correlation between the growth rate, size and morphology was next evaluated using Scanning Electron Microscopy (SEM) and Transmission Electron Microscopy (TEM) (Fig. 2, 3 and S1, ESI†). The growth of ZIF-8 crystals is known to evolve with time from cubes exposing 6 {100} faces to intermediate shapes, and finally to rhombic dodecahedra exposing 12 {110} faces,[23] the latter being most likely the stable equilibrium morphology of ZIF-8 (Fig. 4). With $Zn(acac)_2$, an average size of 45 nm was estimated from SEM and TEM images. Some isolated particles could be observed but the sample mainly constitutes aggregates containing particles with poorly resolved shapes (Fig. 2a and 3a). With $Zn(NO_3)_2$,

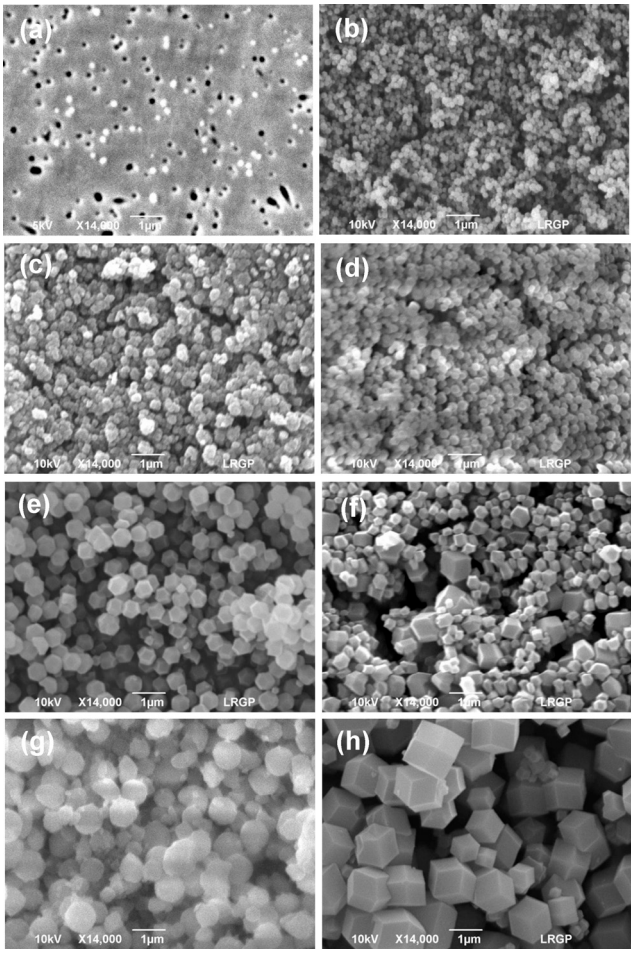

Fig. 2 SEM images of ZIF-8 crystals obtained after 1 h reaction using a Hmim/Zn ratio of 8/1 and starting from (a) $Zn(acac)_2$, (b) $Zn(NO_3)_2$, (c) $ZnSO_4$, (d) $Zn(ClO_4)_2$, (e) $Zn(OAc)_2$, (f) $ZnCl_2$, (g) ZnI_2, and (h) $ZnBr_2$.

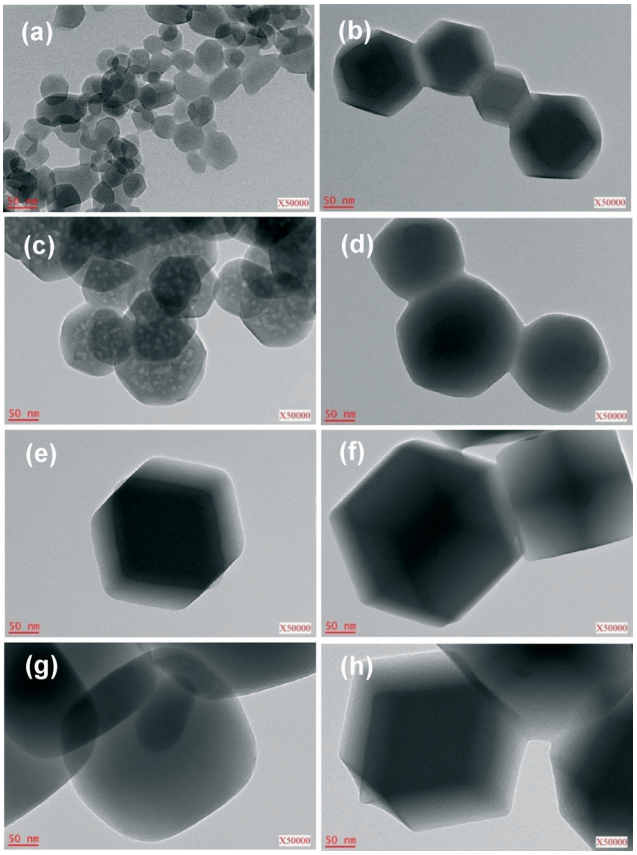

Fig. 3 TEM images of ZIF-8 crystals obtained after 1 h reaction using a Hmim/Zn ratio of 8/1 and starting from (a) $Zn(acac)_2$, (b) $Zn(NO_3)_2$, (c) $ZnSO_4$, (d) $Zn(ClO_4)_2$, (e) $Zn(OAc)_2$, (f) $ZnCl_2$, (g) ZnI_2, and (h) $ZnBr_2$.

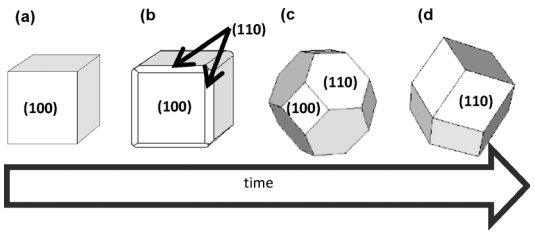

Fig. 4 Illustration of the crystal morphology evolution with time: (a) cube, (b) cube with truncated edges, (c) rhombic dodecahedron with truncated corners, and (d) rhombic dodecahedron.

well-defined truncated rhombic dodecahedral crystals with an average size of 141 ± 48 nm, which is the typical ZIF-8 morphology, were obtained (Fig. 2b and 3b). Small sized (211 ± 60 nm) truncated nanoparticles were obtained from $ZnSO_4$. However, all of the crystals exhibit holes indicating that they are in the stage of dissolution and that Ostwald ripening has likely taken place (Fig. 2c and 3c). Uniformly sized nanoparticles with an average diameter of 224 nm were obtained using $Zn(ClO_4)_2$. The crystals were rather spherical and had bumpy surfaces but some angles could be observed on some of them (Fig. 2d and 3d). Using $ZnCl_2$, larger crystals of *ca.* 300 nm together with many considerably smaller ones (*ca.* 150 nm) can be seen. Both the larger and smaller

Published on 13 March 2014. Downloaded by Gebze Institute of Technology on 14/05/2014 15:56:09.

crystals exhibit cubic and rhombic shapes (Fig. 2f and 3f). With these five reactive zinc precursors (soft Zn^{2+} acid associated with hard bases such as NO_3^- or ClO_4^-), a huge amount of Zn^{2+} ions is available to coordinate with Hmim and the number of nuclei generated by the complex formation is probably large resulting in a decrease in crystal size and crystal anisotropy. This is further supported by the maximum size of the crystals produced in these syntheses. The maximum size decreases because a larger number of nuclei can only grow to a smaller individual crystal size and the growth is stopped due to a rapid decrease in supersaturation. With $Zn(OAc)_2$ and ZnI_2, the particles had the typical rhombic dodecahedron shape and their mean size is *ca.* 500 nm. The images show also that the particles have good uniformity, well-defined facets and sharp edges and corners (Fig. 2e, 3e and Fig. 2g, 3g). It is also worth mentioning that the hydration degree of $Zn(OAc)_2$ (anhydrous $Zn(OAc)_2$ *vs.* $Zn(OAc)_2{\cdot}2H_2O$) has no effect on the size and morphology of ZIF-8 crystals produced (data not shown). The largest nanocrystals, *ca.* 1050 nm in size, were observed with $ZnBr_2$ (Fig. 2h and 3h). Separated large grains with a rhombic dodecahedron shape were obtained together with cubes. All of the particles have well-defined facets and sharp edges and corners. For this zinc precursor with lower reactivity (soft Zn^{2+} acid associated with the soft Br^- base), the density of nuclei is reduced and nanoparticles grow through further direct addition of single monomeric mim^- and solvated Zn^{2+} ion species until the framework is formed.

The particle size was further studied by dynamic light scattering (DLS). The DLS-determined mean particle size values of 85, 192, 247, 312, 480, 388, 589 and 1160 nm obtained for ZIF-8 crystals prepared from $Zn(acac)_2$, $Zn(NO_3)_2$, $ZnSO_4$, $Zn(ClO_4)_2$, $Zn(OAc)_2$, $ZnCl_2$, ZnI_2 and $ZnBr_2$, respectively, are in relatively good agreement with the TEM and SEM determined values (Fig. S2, ESI†).

Thermogravimetric analyses coupled to mass spectrometry (TGA/MS) were conducted on three representative samples prepared from $Zn(NO_3)_2$, $Zn(OAc)_2$ and $ZnBr_2$ to gain information about the thermal stability of ZIF-8 nanocrystals (Fig. 5). From 20 to 250 °C, the TGA curves exhibited only a very weak weight loss of less than 0.5%, corresponding to the removal of guest molecules (methanol or Hmim) and/or CO_2 from the cavities as indicated by MS analyses. A long plateau was then observed after the formation of the guest-free phase $Zn(mim)_2$ until 350 °C, indicating good thermal stability of the three-dimensional network for all samples, which is comparable to that in the literature.[13] Since nearly no weight loss is seen by TGA until 350 °C before the onset of the exothermic decomposition of the mim bridging ligand, it is clear that the solvent or unreacted species have left the intracrystalline cavities during workup and that the synthetic protocol used affords highly pure nanocrystals that do not need solvent exchange and extensive drying for further use. The most significant feature observed in the TGA results is the size-dependent thermal stability up to 300 °C in the case of the smaller 141 nm sized nanocrystals prepared from $Zn(NO_3)_2$, and up to 390 °C in the case of the larger 1050 nm sized crystals prepared from $ZnBr_2$. A sharp weight loss step of *ca.* 63–64% was observed for all nanocrystals upon further increasing the temperature from 400 to 500 °C, indicating thermal decomposition of ZIF-8 nanocrystals in that temperature range. This weight loss is in good agreement with the theoretical weight loss of 64% and indicates that zinc oxide [ZnO, Fw = 81] was formed as the final calcination product of ZIF-8 nanocrystals [$Zn(mim)_2$; Fw = 229] (see Fig. S3 in the ESI† for the XRD pattern of the product obtained, which is in good accordance with the ZnO reference pattern, JCPDS card no 79-2205).

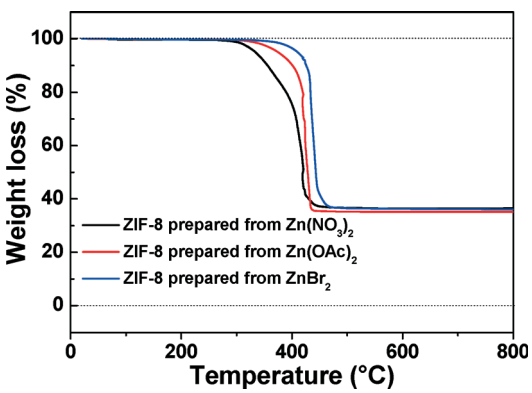

Fig. 5 TGA curves of ZIF-8 nanocrystals prepared from $Zn(NO_3)_2$ (black line), $Zn(OAc)_2$ (red line), and $ZnBr_2$ (blue line).

The N_2 sorption properties of ZIF-8 samples prepared with $Zn(NO_3)_2$, $Zn(OAc)_2$, and $ZnBr_2$ were next investigated (Fig. 6). It was found that they exhibited typical type-I adsorption isotherms with a high level of N_2 adsorption, indicating the microporous nature of the crystals. This was confirmed by the increase in the volume adsorbed at low relative pressures ($P/P_0 < 0.08$). The specific surface area and micropore volume of the ZIF-8 crystals prepared from $Zn(NO_3)_2$ were 1700 ± 30 $m^2\ g^{-1}$ and 0.66 $cm^3\ g^{-1}$, values in perfect accordance with those in the literature (S_{BET} = 1700 $m^2\ g^{-1}$ and V_{micro} = 0.64 $cm^3\ g^{-1}$).[13] Similar results were obtained with crystals prepared from $ZnBr_2$ (S_{BET} = 1713 ± 45 $m^2\ g^{-1}$ and V_{micro} = 0.63 $cm^3\ g^{-1}$). The BET surface areas of nanocrystals and pore volumes prepared from $Zn(OAc)_2$ appear lower than those prepared from $Zn(NO_3)_2$ and $ZnBr_2$ (S_{BET} = 1477 ± 36 $m^2\ g^{-1}$ and V_{micro} = 0.55 $cm^3\ g^{-1}$). The adsorption–desorption hysteresis loop of N_2 near P/P_0 = 1, which originates from interparticle mesopores,[35] is consistent with the interparticle voids observed by SEM and demonstrates the dual micro- and mesoporosity of ZIF-8 nanoparticles. It can further be observed that the adsorbed N_2 amount near P/P_0 = 1 increased for ZIF-8 crystals prepared with $Zn(NO_3)_2$ and $Zn(OAc)_2$ compared to the sample prepared from $ZnBr_2$. These results suggest that the interparticle porosity between ZIF-8 crystals produced from $Zn(NO_3)_2$ and $Zn(OAc)_2$ increases due to the decrease in particle size and confirms the SEM and TEM results (*vide supra*).

 This journal is © The Royal Society of Chemistry 2014

Published on 13 March 2014. Downloaded by Gebze Institute of Technology on 14/05/2014 15:56:09.

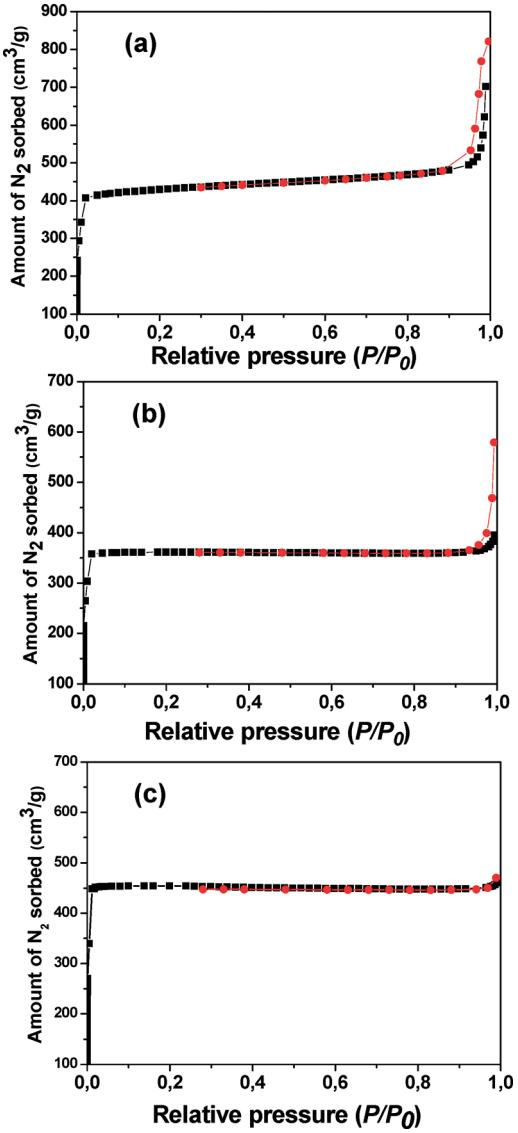

Fig. 6 Nitrogen sorption isotherms measured at 77 K on the powder ZIF-8 crystals obtained from (a) $Zn(NO_3)_2$, (b) $Zn(OAc)_2$, and (c) $ZnBr_2$. Black and red data correspond to the adsorption and desorption branches, respectively.

In the last set of experiments, we evaluated the catalytic properties of ZIF-8 crystals produced from $Zn(NO_3)_2$, $Zn(OAc)_2$, and $ZnBr_2$. A Knoevenagel reaction between 4-bromobenzaldehyde and malononitrile, which is well-established for ZIF-8 crystals, was first studied.[36–38] Condensation was conducted for 5 h at room temperature and isolated yields of 2-(4-bromobenzylidene)malononitrile are reported in Fig. 7. As can be seen, the reaction worked effectively with the three catalysts but was only complete with ZIF-8 crystals produced from $Zn(NO_3)_2$.

Fig. 8 shows the conversion of 4-bromobenzaldehyde when reacting with malononitrile in the presence of the different-sized ZIF-8 crystals as a function of time. As can be seen, condensation proceeds very quickly at room temperature and is almost quantitative (96%) after 30 min when

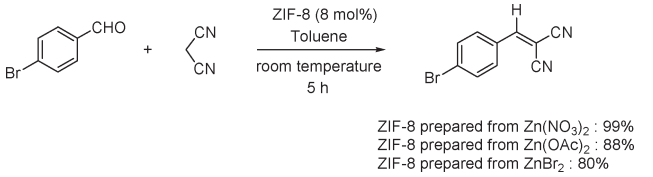

Fig. 7 Catalytic activities of ZIF-8 crystals prepared from different zinc sources in the Knoevenagel reaction.

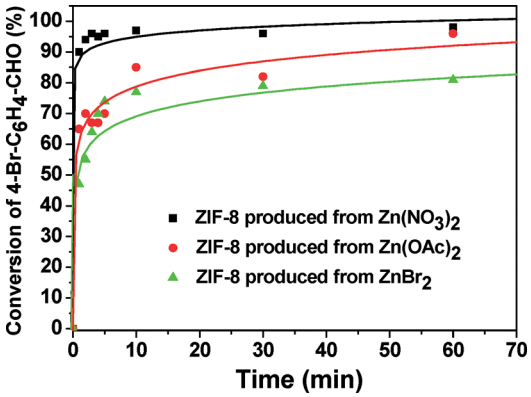

Fig. 8 Time-dependent conversion plots for the Knoevenagel reaction between 4-bromobenzaldehyde and malononitrile catalyzed by ZIF-8 crystals (reactions were conducted in toluene at room temperature).

catalyzed by ZIF-8 crystals produced from $Zn(NO_3)_2$. With ZIF-8 crystals prepared from $Zn(OAc)_2$ and $ZnBr_2$, the reaction proceeded with more difficulty, though conversions of 82 and 79% were observed after 30 min, thus indicating the importance of the ZIF-8 crystal size in the reaction. It should also be noted that significantly longer reaction times (5 h) were required for the reaction using the latter catalysts.

The catalytic performance of the different-sized ZIF-8 crystals was next evaluated in the Friedländer reaction between 2-aminobenzophenone and acetylacetonate. The Friedländer reaction is an important synthetic approach to prepare quinoline derivatives,[39,40] heterocycles possessing a wide range of pharmaceutical and biological activities.[41] Cu(BDC) and Cu(BTC) MOFs (BDC = 1,4-benzenedicarboxylic acid, BTC = 1,3,5-benzenetricarboxylic acid) have already been demonstrated to be efficient catalysts for the Friedländer reaction.[42–45] As can be seen in Fig. 9, the 2-quinolone derivative can be obtained in moderate to excellent yields using ZIF-8 crystals as catalysts and the highest catalytic activity

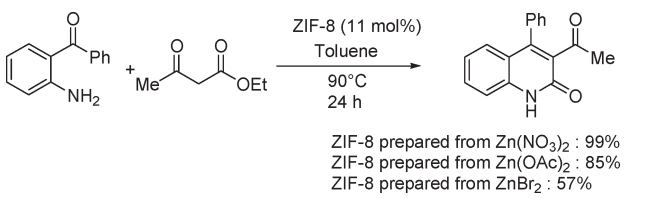

Fig. 9 Catalytic activities of ZIF-8 crystals prepared from different zinc sources in the Friedländer reaction.

Published on 13 March 2014. Downloaded by Gebze Institute of Technology on 14/05/2014 15:56:09.

was as previously observed for the smallest ZIF-8 crystals prepared from $Zn(NO_3)_2$.

In both catalytic experiments, the conversion of the starting materials increased over ZIF-8 crystals in the following sequence: ZIF-8 from $Zn(NO_3)_2$ > ZIF-8 from $Zn(OAc)_2$ > ZIF-8 from $ZnBr_2$. The reduced catalytic activity with the decrease in the external surface area of the ZIF-8 crystals is probably linked to the increase in adsorption rates of nanocrystals compared to microcrystals, as recently observed with metal–organic framework nanofibers,[46] and to the increasing concentration of accessible Lewis acid and basic sites at the surface of the smallest nanoparticles.

Conclusions

In conclusion, we demonstrated that phase pure ZIF-8 crystals can be produced from Hmim and various zinc sources in methanol at room temperature. The reactivity of the zinc salt in the growth solution was found to markedly affect the size and morphology of ZIF-8 particles produced after 1 h reaction and at the same concentration of the zinc salt. Small ZIF-8 nanocrystals with diameters varying between *ca.* 50 and 200 nm were obtained with reactive zinc salts like $Zn(acac)_2$, $Zn(NO_3)_2$, $ZnSO_4$ or $Zn(ClO_4)_2$. The use of $ZnCl_2$, $Zn(OAc)_2$ or ZnI_2 afforded crystals with sizes varying between *ca.* 350 and 650 nm. Finally, the use of the low reactive $ZnBr_2$ was found to generate microsized crystals. These significant changes in particle size induced distinctive changes in the adsorption properties as demonstrated by BET measurements but also in the catalytic performance of ZIF-8 crystals in Knoevenagel and Friedländer condensation reactions used as models. The small sized crystals produced from $Zn(NO_3)_2$ exhibited the highest surface area and the best catalytic activity. Our results should open new opportunities to control the reactivity of ZIF-8 crystals in applications such as films and membranes.

Experimental

Materials

The chemicals used in the experiments were zinc acetate dihydrate (98+%, Aldrich), anhydrous zinc acetate (99.99%, Aldrich), zinc bromide (98%, Riedel de Haën), zinc chloride (98%, Aldrich), zinc nitrate hexahydrate (98%, Aldrich), zinc perchlorate hexahydrate (Aldrich), zinc sulphate heptahydrate (99%, Merck), 2-methylimidazole (Hmim, 99%, Aldrich), 4-bromobenzaldehyde (99%, Aldrich), malononitrile (99%, Aldrich), ethyl acetoacetate (99%, Aldrich), 2-aminobenzophenone (98%, Aldrich), toluene (99%, Prolabo), and methanol (≥99.9%, Aldrich).

General information

Transmission electron microscopy (TEM) images were taken by placing a drop of the ZIF-8 particles in methanol onto a carbon film-supported copper grid. Samples were studied using a Philips CM20 instrument operating at 200 kV. Scanning electron microscopy (SEM) pictures were prepared using a JEOL scanning electron microscope JSM-6490 LV. The ZIF-8 material prepared from zinc acetylacetonate was viewed on an Isopore™ membrane (Merck Millipore) with 0.2 μm pore size. The X-ray powder diffraction (XRD) diagrams of all samples were measured using a PANalytical X'Pert Pro MPD diffractometer using Cu Kα radiation. The X-ray powder diffraction data were collected using an X'Pert MPD diffractometer (PANalytical AXS) with a goniometer radius of 240 mm, a fixed divergence slit module (1/2° divergence slit, 0.04 rad Soller slits) and an X'Celerator as a detector. The powder samples were placed on a silicon zero-background sample holder and the XRD patterns were recorded at room temperature using Cu K_α radiation (λ = 0.15418 nm). DLS measurements were performed on a ZEN 3600 Zetasizer Nano ZS. The solid materials were redispersed in methanol by sonication and transferred to quartz cuvettes through a syringe. The textural properties of the materials were investigated using a Micromeritics ASAP 2420 instrument using liquid nitrogen (−196 °C). Prior to analyses, the samples were outgassed overnight in vacuum at 40 °C on the degassing port followed by 4 h of out-gassing on the analysis port. The resulting isotherms were analysed using the BET (Brunauer–Emmett–Teller) method while the micropore volume (V_{micro}) was determined using the Horvath–Kawazoe (HK) equation. Thermogravimetric measurements were performed on a SETARAM Setsys Evolution thermoanalyzer coupled with an OmniStar GSD301C-Pfeiffer Vacuum mass spectrometer. Samples were filled into platinum crucibles and heated in flowing air with a ramp of 5 °C min^{-1} from room temperature up to 800 °C. ^1H NMR spectra were recorded in $CDCl_3$ using a 300 MHz spectrometer (Avance 300, Bruker, Bremen, Germany). Chemical shift values were reported in ppm relative to the residual peak of the solvent.

Synthesis of ZIF-8 crystals

Solutions of the Zn^{2+} salt (1 mmol) and Hmim (660 mg, 8 mmol) in 11.3 mL of methanol were prepared separately. Then, in a three-neck-flask, the two solutions were mixed by dropwise addition of the Hmim solution to the Zn^{2+} salt solution. Synthesis was conducted under nitrogen flow at room temperature with stirring for 1 h. The ZIF-8 crystals were separated by centrifugation (4000 rpm, 15 min) and washed with methanol (3 × 30 mL). The nanocrystals were dried in air overnight before analysis.

Catalytic experiments

The ZIF-8 samples were activated by treatment of the powders at 200 °C in a programmable oven for 6 h, and then cooled to room temperature naturally. The vials containing the ZIF-8 powders were tightly capped and stored at room temperature before use.

Knoevenagel condensation. 4-Bromobenzaldehyde (0.0925 g, 0.5 mmol) was dissolved in 5 mL of toluene, the ZIF-8 catalyst (9.2 mg, 0.04 mmol) was added and the mixture was stirred for

 This journal is © The Royal Society of Chemistry 2014

Published on 13 March 2014. Downloaded by Gebze Institute of Technology on 14/05/2014 15:56:09.

5 min. Malononitrile was then injected (0.189 mL, 3 mmol) and the reaction was conducted with bubbling of Ar gas through the mixture for 5 h at room temperature. After centrifugation and concentration of the toluene phase, the crude reaction mixture was purified using silica gel column chromatography (petroleum ether–ethyl acetate (v/v), 95 : 5) and the product was analyzed by ^{1}H NMR. ^{1}H NMR ($CDCl_3$, 300 MHz): δ 7.74 (d, J = 8.7 Hz, 2H), 7.73 (s, 1H), 7.67 (d, J = 8.7 Hz, 2H).

Friedländer condensation. 2-Aminobenzophenone (82.1 mg, 0.42 mmol) and ethyl acetoacetate (81.3 mg, 0.62 mmol) were added to ZIF-8 crystals (16 mg, 0.069 mmol) dispersed in 2 mL of toluene. The mixture was heated at 90 °C and the progress of the reaction was monitored by TLC. After cooling, the reaction mixture was centrifuged and the toluene phase was concentrated. The crude product was purified using silica gel chromatography (petroleum ether–ethyl acetate (v/v), 95 : 5) and the product was analyzed by ^{1}H NMR. ^{1}H NMR ($CDCl_3$, 300 MHz): δ 12.05 (s, NH), 7.58–7.13 (m, 9H), 2.31 (s, 3H).

Acknowledgements

This work was supported by the ICCEL and MICA Carnot Institutes. We thank Jean-François Remy (LRGP, CNRS) for SEM analyses and Anne Sapin-Minet (EA 3452, Cithéfor, Université de Lorraine) for DLS measurements.

Notes and references

1 J. S. Seo, D. Whang, H. Lee, S. I. Jun, J. Oh, Y. J. Jeon and K. Kim, *Nature*, 2000, **404**, 982.
2 M. Muller, S. Hermes, K. Kaehler, M. W. E. van den Berg, M. Mahler and R. A. Fischer, *Chem. Mater.*, 2008, **20**, 4576.
3 F. Gandora, E. G. Puebla, M. Iglesias, D. M. Proserpio, N. Shejko and M. A. Monge, *Chem. Mater.*, 2009, **21**, 655.
4 L. Q. Ma, J. Y. Lee, J. Li and W. B. Lin, *Inorg. Chem.*, 2008, **47**, 3955.
5 R. E. Morris and P. S. Wheatley, *Angew. Chem., Int. Ed.*, 2008, **47**, 4966.
6 Y. H. Hu and L. Zhang, *Adv. Mater.*, 2010, **22**, E117.
7 P. K. Thallapally, J. Tian, M. R. Kishan, C. A. Fernandez, S. J. Dalgarho, P. B. Mc Grail, J. E. Warren and J. L. Atwood, *J. Am. Chem. Soc.*, 2008, **130**, 16842.
8 A. O. Yazaydin, R. Q. Snurr, T.-H. Park, K. Koh, J. Liu, M. D. LeVan, A. I. Benin, P. Jakubczak, M. Lanuza, D. B. Galloway, J. J. Low and R. R. Willis, *J. Am. Chem. Soc.*, 2009, **131**, 18198.
9 B. Wang, A. P. Côté, H. Furukawa, M. O'Keeffe and O. M. Yaghi, *Nature*, 2008, **453**, 207.
10 R. Banerjee, A. Phan, B. Wang, C. Knobler, H. Furukawa, M. O'Keeffe and O. M. Yaghi, *Science*, 2008, **319**, 939.
11 H. Hayashi, A. P. Côté, H. Furukawa, M. O'Keeffe and O. M. Yaghi, *Nat. Mater.*, 2007, **6**, 501.
12 H. Wu, W. Zhou and T. Yildirim, *J. Am. Chem. Soc.*, 2007, **129**, 5314.
13 K. S. Park, Z. Ni, A. P. Côté, J. Y. Choi, R. D. Huang, F. J. Uribe-Romo, H. K. Chae, M. O'Keeffe and O. M. Yaghi, *Proc. Natl. Acad. Sci. U. S. A.*, 2006, **103**, 10186.
14 H. Wu, W. Zhou and T. Yildirim, *J. Am. Chem. Soc.*, 2009, **131**, 4995.
15 J. Pérez-Pellitero, H. Amrouche, F. R. Siperstein, G. Pirngruber, C. Nieto-Draghi, G. Chaplais, A. Simon-Masseron, D. Bazer-Bachi, D. Peralta and N. Bats, *Chem. – Eur. J.*, 2010, **16**, 1560.
16 S. R. Venna and M. A. Carreon, *J. Am. Chem. Soc.*, 2010, **132**, 76.
17 R. Krishna and J. M. van Baten, *J. Membr. Sci.*, 2010, **360**, 323.
18 A. S. Huang, H. Bux, F. Steinbach and J. Caro, *Angew. Chem., Int. Ed.*, 2010, **49**, 4958.
19 P. Küsgens, M. Rose, I. Senkovska, H. Fröde, A. Henschel, S. Siegle and S. Kaskel, *Microporous Mesoporous Mater.*, 2009, **120**, 325.
20 K. A. Cychosz and A. J. Matzger, *Langmuir*, 2010, **26**, 17198.
21 J. Cravillon, R. Nayuk, S. Springer, A. Feldhoff, K. Huber and M. Wiebcke, *Chem. Mater.*, 2011, **23**, 2130.
22 J. Cravillon, C. A. Schröder, R. Nayuk, J. Gummel, K. Huber and M. Wiebcke, *Angew. Chem.*, 2011, **123**, 8217.
23 J. Cravillon, C. A. Schröder, H. Bux, A. Rothkirch, J. Caro and M. Wiebcke, *CrystEngComm*, 2012, **14**, 492.
24 M. Shah, H. T. Kwon, V. Tran, S. Sachdeva and H.-K. Jeong, *Microporous Mesoporous Mater.*, 2013, **165**, 63.
25 S. K. Nune, P. K. Thallapally, A. Dohnalkova, C. Wang, J. Liu and C. J. Exarhos, *Chem. Commun.*, 2010, **46**, 4878.
26 Y. Pan, D. Heryadi, F. Zhou, L. Zhao, G. Lestari, H. Su and Z. Lai, *CrystEngComm*, 2011, **13**, 6937.
27 A. Garai, W. Shephard, J. Huo and D. Bradshaw, *J. Mater. Chem. B*, 2013, **1**, 3678.
28 E. Biemmi, S. Christian, N. Stock and T. Bain, *Microporous Mesoporous Mater.*, 2009, **117**, 111.
29 N. L. Torad, M. Yu, Y. Kamachi, K. Takai, M. Imura, N. Naito and Y. Yamauchi, *Chem. Commun.*, 2013, **49**, 2521.
30 M. Zhu, S. R. Venna, J. B. Jasinski and M. A. Carreon, *Chem. Mater.*, 2011, **23**, 3590.
31 J. Cravillon, S. Munzer, S. J. Lohmeier, A. Feldhoff, K. Huber and M. Wiebcke, *Chem. Mater.*, 2009, **21**, 1410.
32 H. Bux, F. Liang, Y. Li, J. Cravillon, M. Wiebcke and J. Caro, *J. Am. Chem. Soc.*, 2009, **131**, 16000.
33 S. R. Venna, J. B. Jasinski and M. A. Carreon, *J. Am. Chem. Soc.*, 2010, **132**, 18030.
34 L. Ratke and P. W. Voorhes, *Growth and Coarsening: Ripening in Material Processing*, Springer, Berlin, 2002, p. 117.
35 K. S. W. Sing, D. H. Everett, R. A. W. Haul, L. Moscou, R. A. Pierotti, J. Rouquérol and T. Siemieniewska, *Pure Appl. Chem.*, 1985, **57**, 603.
36 V. P. N. Tran, K. K. Le and N. T. S. Phan, *ACS Catal.*, 2011, **1**, 120.
37 H.-Y. Cho, J. Kim, S.-N. Kim and W.-S. Ahn, *Microporous Mesoporous Mater.*, 2013, **169**, 180.
38 R. Jin, Z. Bian, J. Li, M. Ding and L. Gao, *Dalton Trans.*, 2013, **42**, 3936.

Published on 13 March 2014. Downloaded by Gebze Institute of Technology on 14/05/2014 15:56:09.

39 R. Ostermann, J. Cravillon, C. Weidmann, M. Wiebcke and B. M. Smarsly, *Chem. Commun.*, 2011, **47**, 442.
40 M. Barbero, S. Bazzi, S. Cadamuro and S. Dughera, *Tetrahedron Lett.*, 2010, **51**, 2342.
41 P. G. Dormer, K. K. Eng, R. N. Farr, G. R. Humphrey, J. C. Mc Williams, P. J. Reider, J. W. Sager and R. P. Volante, *J. Org. Chem.*, 2003, **68**, 467.
42 J. Marco-Contelles, E. Pérez-Mayoral, A. Samadi, M. do Carmo Carreiras and E. Soriano, *Chem. Rev.*, 2009, **109**, 2652.
43 E. Pérez-Mayoral and J. Cejka, *ChemCatChem*, 2011, **3**, 157.
44 E. Pérez-Mayoral, Z. Musilova, B. Gil, B. Marszalek, M. Polozij, P. Nachtigall and J. Cejka, *Dalton Trans.*, 2012, **41**, 4036.
45 N. T. S. Phan, T. T. Nguyen, K. D. Nguyen and A. X. T. Vo, *Appl. Catal., A*, 2013, **464–465**, 128.
46 R. Ostermann, J. Cravillon, C. Weidmann, M. Wiebcke and B. M. Smarsly, *Chem. Commun.*, 2011, **47**, 442.

 This journal is © The Royal Society of Chemistry 2014